Draft version April 7, 2025
Typeset using LaTeX **twocolumn** style in AASTeX631

A MULTIWAVELENGTH AUTOPSY OF THE INTERACTING IIN SUPERNOVA 2020YWX: TRACING ITS PROGENITOR MASS-LOSS HISTORY FOR 100 YEARS BEFORE DEATH

Raphael Baer-way [1,2] Poonam Chandra [2] and Maryam Modjaz [1]

[1] *Department of Astronomy, University of Virginia, Charlottesville VA 22904-4325, USA*
[2] *National Radio Astronomy Observatory, 520 Edgemont Rd, Charlottesville VA 22903, USA*

ABSTRACT

While the subclass of interacting supernovae with narrow hydrogen emission lines (SNe IIn) consists of some of the longest-lasting and brightest SNe ever discovered, their progenitors are still not well understood. Investigating SNe IIn as they emit across the electromagnetic spectrum is the most robust way to understand the progenitor evolution before the explosion. This work presents X-ray, optical, infrared, and radio observations of the strongly interacting Type IIn SN 2020ywx covering a period > 1200 days after discovery. Through multiwavelength modeling, we find that the progenitor of 2020ywx was losing mass at $\sim 10^{-2}$–$10^{-3}\,\mathrm{M_\odot\,yr^{-1}}$ for at least 100 yrs pre-explosion. Furthermore, we find evidence for dust formation in the shocked region. Based on the observed elevated mass loss over more than 100 years and the configuration of the CSM inferred from the multiwavelength observations, we invoke binary interaction as the most plausible mechanism to explain the overall mass-loss evolution. SN 2020ywx is thus a case that may support the growing observational consensus that SNe IIn mass loss is explained by binary interaction.

1. INTRODUCTION

Interacting supernovae (SNe) are defined by significant interaction between the exploding star's ejecta and the dense surrounding circumstellar matter (CSM) expelled during the late stages of the progenitor star's life. This interaction generates shocks which create sustained emission across the electromagnetic spectrum from the radio to the X-rays (Chevalier & Fransson 2017; Chugai & Danziger 1994). Most interacting SNe are Type IIn supernovae (SNe IIn; Smith 2017), with Schlegel (1990) being the first to note and classify the defining narrow hydrogen emission lines in SNe IIn (for a full overview of SN subtypes see Filippenko 1997, Gal-Yam et al. 2021, and Modjaz et al. 2019). While SNe IIn constitute between $\sim 5\%$ (Cold & Hjorth 2023) to 9% (Smith et al. 2011a) of core-collapse SNe (with many evolving subtypes (Yesmin et al. 2024)), the progenitor class that gives rise to these objects is relatively unconstrained.

The most significant piece of evidence used to make deductions about SN IIn progenitors is the star's pre-explosion mass-loss rate. The mass-loss rates measured for SNe IIn range from $\sim 10^{-4}$ to $10^{0}\,\mathrm{M_\odot\,yr^{-1}}$ (Taddia et al. 2013), which pushes the limit for single-star wind-driven mass loss well past the breaking point of $\sim 10^{-4}\,\mathrm{M_\odot\,yr^{-1}}$ (Smith & Owocki 2006). Luminous blue variables (LBVs) are the only observed class of star that could produce such high (and relatively fast at $> 100\,\mathrm{km\,s^{-1}}$) mass-loss rates (Smith 2014; Smith & Owocki 2006; Smith 2017; Taddia et al. 2013), although it is now suspected that many LBVs originate in binaries (see, e.g., Aghakhanloo et al. 2023; Smith & Tombleson 2015). While LBVs can match the measured mass-loss rates, it is unclear why a star would explode directly after the LBV phase, when traditional single-star models with strong mass loss expect LBVs to enter a Wolf-Rayet phase (for potentially $> 10,000$ yr before the explosion, depending on initial mass) where it would lose nearly all of its hydrogen (Heger et al. 2003). Nevertheless, there has been direct observational evidence of LBVs exploding as SNe IIn (e.g., SN 2005gl, Gal-Yam et al. 2007; SN 2009ip, Mauerhan et al. 2013).

This is not to say that every case of high mass loss is associated with an LBV progenitor. Reguitti et al. (2024) found from a limited sample that only $\sim 30\%$ of SNe IIn had pre-SN, LBV-like outbursts. Wave-driven instabilities, pulsational pair instabilities, and binary interaction are other potential mechanisms that may produce the requisite mass loss for SNe IIn (Woosley 2017; Smith et al. 2007; Taddia et al. 2013; Smith & Arnett 2014; Quataert & Shiode 2012; Wu & Fuller 2021). However, for nearly all SNe IIn, the predictions of the pulsational pair instability do not match observed spectral properties (Woosley & Smith 2022; Smith et al. 2023), and the very brief ∼1 yr timescale for wave-driven mass loss (Quataert & Shiode 2012; Wu & Fuller 2021) falls far short of the sustained high mass loss needed for decades to centuries in most SNe IIn (Smith et al. 2023). This favors violent binary interaction as a primary agent for the strong pre-SN mass loss (Smith & Arnett 2014). In particular, recent work investigating spectropolarimetry of SNe IIn (Bilinski et al. 2024) has suggested that some kind of binary interaction leading to asymmetric CSM may be the leading cause of pre-explosion mass loss in SNe IIn.

CSM interaction in SNe is associated with dust formation as well. Infrared (IR) spectra of SNe IIn have revealed strong blackbody emission, providing robust confirmation for the presence of dust (Fox et al. 2011). Despite differing arguments about the location of the dust, it is difficult to dispute that dust forms in the dense shell of many SNe IIn based on progressively more observational evidence (Gall et al. 2014; Smith et al. 2023).

To better probe the shock physics and the structure within the CSM and ejecta, radio and X-ray emission can provide a more detailed picture. Interacting SNe are the only SN subtype expected to produce long-lasting radio emission in the form of synchrotron radiation from the accelerated electrons in the forward shock (the shock moving outwards into the CSM) (Chevalier 1982).

Extensive modeling and analysis has been done to paint the theoretical picture of these dense radio-producing shocks. Chandra (2018) and Chevalier & Fransson (2017) give a broad overview of the different types of absorption expected (synchrotron self-absorption or free-free absorption). An understanding of the absorption mechanism from observational data is significant as it allows for an estimate of the pre-explosion mass-loss rate.

In the X-rays, the general picture in most interacting SNe is that the heating from a collisionless shock will generate thermal photons hot enough to emit X-rays (Chevalier & Fransson 2017; Margalit et al. 2022). X-ray observations of interacting SNe and SNe in general are critical owing to the wealth of information they reveal about element abundances, the ejecta, and CSM density structure as well as the presence of ionized/neutral lines which provide information about the density and state of the shock (Dwarkadas et al. 2016).

Thus, the X-ray, radio, and optical results can be combined to paint an overall picture of the pre-SN evolution from hundreds to thousands of years pre-explosion up to the explosion date itself. This is what we seek to do in this work for SN 2020ywx, an object for which we obtained extensive radio, near-IR (NIR), optical, and X-ray data. We obtained radio data with the Very Large Array, X-ray data from Chandra and Swift, and optical data form the Arizona LBT telescope and Magellan Telescopes in Chile.

2. ANALYSIS

2.1. *X-Ray Data Analysis*

We performed fits to the reduced X-ray data of SN 2020ywx to determine the best-fitting model. The best fit (as measured by χ^2) was found by fitting each *Chandra* X-ray spectrum of SN 2020ywx with a thermal plasma model (xspec's *apec*) at Solar abundance (having no way to accurately constrain the host metallicity) with additional Gaussians associated with line emission. This best-fitting model is expected as the X-ray emission originates from shock heating of the particles by the collisionless shock, especially at later times. The best-fit parameters are shown in Table 1.

2.2. *Optical/IR*

The optical light curve of SN 2020ywx covers a period of 1200 days and is striking in the remarkably constant linear decline for > 1000 days post-explosion. We fit the light curve with a linear function using MCMC fitting and find a decay rate of $0.00333^{+0.000015}_{-0.000016}\,\mathrm{mag\,day^{-1}}$ in the ZTF r band and $0.00455^{+0.00003}_{-0.00003}\,\mathrm{mag\,day^{-1}}$ in the ZTF g band. The difference in decline in the two bands is likely due to the strong Hα emission contributing to the r-band measurements.

After fitting the lightcurve, we proceeded to fit the spectra of SN 2020ywx. To capture the Hα emission, we attempted Gaussian, Lorentzian, and combined Voigt fits (Dessart & Hillier 2022). We performed Monte Carlo Markov Chain (MCMC) fitting on all spectra. We use the `emcee` package (Foreman-Mackey et al. 2013), checking for convergence via the stretch statistic.

The Gaussian fits were significantly better, providing a better fit both by visual inspection and by χ^2 (by a factor of > 2). We thus proceeded with MCMC Gaussian fitting.

An example of our fits to one of our spectra with the posterior chains is plotted in Figure 2. A portion of the fitting results that show the general evolution are given in Table 2. The upper and lower error bars are 1σ from the MCMC posterior distributions. We interpret the evolution and widths of the line components in the optical portion of § 3.

The three Near Infrared(NIR) spectra of SN 2020ywx have similarities with the optical spectra in that they are marked by narrow and intermediate-width emission lines. We fit to hydrogen and helium lines again using MCMC methods. Of particular note is the dramatic P Cygni profile in the helium $1.083\,\mu m$ line in the NIRES February 2022 spectrum. We measure a full width at

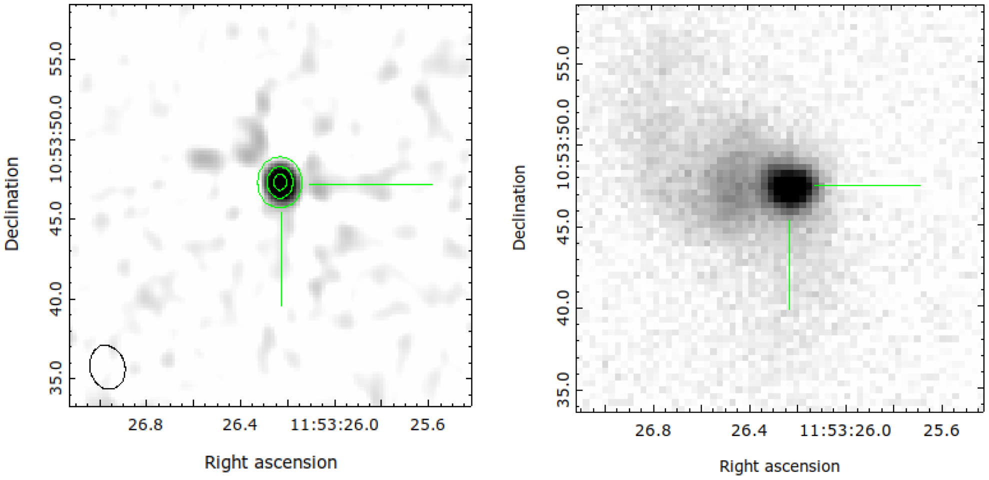

Radio 5 GHz VLA image 11/2021 LCO Optical r-band image 12/2021

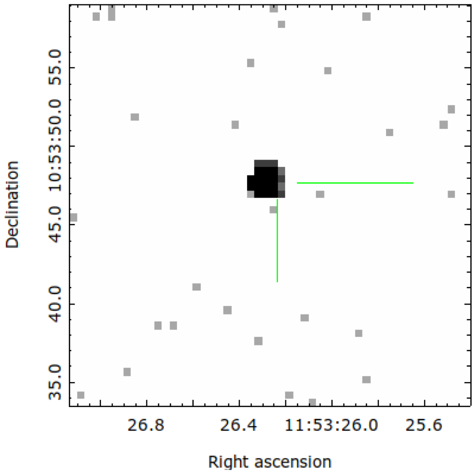

Chandra ACIS-S image 11/2021

Figure 1. Radio, optical, and X-ray images of SN 2020ywx all taken ~ 500 days post-explosion. The crosshairs point at the reported location of the SN (Srivastav et al. 2020). North is up and east is to the left. We emphasize the lack of emission from the host galaxy at radio and X-ray wavelengths. The beam size is shown in the radio image at 5 GHz in the lower-left corner. We additionally show 0.5 mJy contours in the radio image. We note that the host galaxy is not detected at all radio frequencies, including down to 0.4 GHz.

half-maximum intensity (FWHM) of this emission line of $115^{+21}_{-26}\,\mathrm{km\,s^{-1}}$. This is quite close to the speed as measured from the absorption trough of the Hα P Cygni line. Given this measurement, we assume that the CSM speed is not changing over time, given that we find an almost identical value at epochs 150 days apart.

2.3. *Radio*

In interacting SNe, radio emission arises as nonthermal synchrotron emission from relativistically accelerated electrons in the forward shock. This emission occurs in a region exterior to the SN photosphere in the forward-shock region (Chevalier 1982; Weiler et al. 1986). However, it is expected to be absorbed either by synchrotron self-absorption (SSA) or free-free absorption (FFA). The varying optical depth across frequency creates the two regions in the spectrum of a radio SN: the optically thin declining emission and optically thick rising emission. Lower frequency emission is highly attenuated at early times; but as the optical depth decreases with time, eventually the entire radio spectrum becomes optically thin.

We assume a self-similar synchrotron model, as detailed by Chevalier (1982), where the shock radius evolves as $r \propto t^m$, with m related to the ejecta density gradient by $m = (n-3)/(n-s)$. Here, s gives the density structure of the CSM as $\rho_{\rm CSM} \propto r^{-s}$ and n is

Table 1. X-Ray Fit Details

Epoch	Model	χ^2/ν	$N_\mathrm{H}(10^{22}\mathrm{cm}^{-2})$	Temperature (keV)	0.2–10 keV Abs. Flux $\left(\frac{\mathrm{ergs}}{\mathrm{cm}^2\,\mathrm{s}}\right)$	Unabs. 0.2–10 keV Flux $\left(\frac{\mathrm{ergs}}{\mathrm{cm}^2\,\mathrm{s}}\right)$
2021-05-01	Thermal Plasma	1.34	$4.37^{+1.11}_{-0.80}$	20 (frozen)	$3.61^{+0.40}_{-0.42} \times 10^{-13}$	$6.17^{+0.90}_{-0.81} \times 10^{-13}$
–	Gaussian	–	–	6.8 (frozen $\sigma = 0.1$)	–	$6.28^{+2.89}_{-3.09} \times 10^{-14}$
2021-11-10	Thermal Plasma	0.96	$1.59^{+0.47}_{-0.39}$	15 (frozen)	$3.78^{+0.43}_{-0.42} \times 10^{-13}$	$5.05^{+0.62}_{-0.59} \times 10^{-13}$
–	Gaussian	–	–	6.8($\sigma = 0.45$ (frozen)	–	$1.33^{+0.41}_{-1.11} \times 10^{-13}$
–	Gaussian	–	–	3.8($\sigma = 0.3$ (frozen))	–	$1.94^{+1.10}_{-2.7} \times 10^{-14}$
2023-03-23	Thermal Plasma	1.08	$0.76^{+0.10}_{-0.21}$	$13.598^{+30.315}_{-1.62}$	$2.49^{+0.21}_{-0.09} \times 10^{-13}$	$3.43^{+0.14}_{-0.43} \times 10^{-13}$
2024-01-15	Thermal Plasma	0.84	$0.77^{+0.26}_{-0.26}$	$10.38^{+32.37}_{-2.74}$	$1.83^{+0.11}_{-0.12} \times 10^{-13}$	$2.48^{+0.09}_{-0.31} \times 10^{-13}$

NOTE—X-Ray modeling details. Some of the flux errors on the 2021 data are given by χ^2 1σ contours rather than chain estimation owing to unbounded lower values from the MCMC chains.

Table 2. Optical multicomponent Hα fitting across epochs

Days since explosion	Broad FWHM (km/s)	Narrow FWHM	Intermediate FWHM	[N II] 6584 Å FWHM	[N II] 6548 Å FWHM
83	15360^{+133}_{-132}	520^{+14}_{-14}	2720^{+94}_{-89}	450^{+50}_{-46}	–
189	13390^{+30}_{-29}	80^{+1}_{-1}	2630^{+6}_{-6}	80^{+3}_{-3}	280^{+11}_{-11}
594	4750^{+80}_{-77}	110^{+1}_{-1}	1960^{+7}_{-7}	210^{+16}_{-24}	–
1269	–	100^{+4}_{-4}	1510^{+132}_{-121}	260^{+192}_{-117}	–

NOTE—We provide fitting results which show the general trend across epochs. The results are rounded from the exact fitting results to 3 significant figures to reflect the accuracy of the measurements. The blending with [N II] lines is hard to disentangle through fitting in the lower-resolution spectra. The width of the narrow [N II] components is set by the resolution of the instrument. All velocities are given in km s^{-1}.

Table 3. Best-fit parameters from radio modeling (§ 2). 10% uncertainties added in quadrature to the errorbars of the data due to well-known underestimating of radio errors from CASA's *imfit* routine as described in § 2.

Model	χ^2_ν	K_1	K_2	K_3	α	β	β'	δ	δ'
SSA	2.11	$50.1^{+2.49}_{-2.4}$	$0.04^{+0.002}_{-0.002}$	N/A	$0.88^{+0.02}_{-0.02}$	$0.51^{+0.03}_{-0.03}$	$2.37^{+0.08}_{-0.08}$	N/A	N/A
Int FFA	1.30	$2.30^{+0.08}_{-0.07}$	N/A	$0.34^{+0.03}_{-0.03}$	$1.01^{+0.03}_{-0.03}$	$0.66^{+0.04}_{-0.04}$	N/A	N/A	$1.85^{+0.07}_{-0.07}$
Ext FFA	2.10	$2.92^{+0.07}_{-0.06}$	$0.45^{+0.01}_{-0.01}$	N/A	$1.11^{+0.02}_{-0.02}$	$0.75^{+0.04}_{-0.04}$	N/A	$0.93^{+0.04}_{-0.04}$	N/A
Int+Ext FFA	1.51	$1.43^{+0.04}_{-0.04}$	$0.58^{+0.06}_{-0.05}$	$0.35^{+0.04}_{-0.03}$	$1.14^{-0.03}_{+0.03}$	$0.88^{+0.04}_{-0.04}$	N/A	$1.53^{-0.02}_{+0.05}$	$1.71^{+0.10}_{-0.11}$

given by the ejecta density profile as

$$\rho_\mathrm{ej} \propto \rho_0 \left(\frac{t}{t_0}\right)^{-3} \left(\frac{v}{v_0}\right)^{-n} . \tag{1}$$

We expect s to be ~ 2 for a wind-like constant mass-loss CSM, but examine this assumption given that many SNe IIn have shown different density profiles (Chandra 2018). The absorption effects can be parameterized through the temporal and spectral evolution of the flux. We fit four models to our combined radio data.

We see from Table 3 that the internal FFA model is the best fit for the radio data (with $\chi^2_\nu = 1.3$), and adding the external FFA model (and enforcing a physical value for $\delta = 2.7m$) leads to a worse χ^2_ν. This suggests that the external medium is contributing quite minimally to the absorption. The better fit is made clear from the low-frequency GMRT data points, which reveal a shallow dropoff not accounted for in an SSA or external/external+internal FFA model. By constraining the optical depth through our model at 5 GHz, we

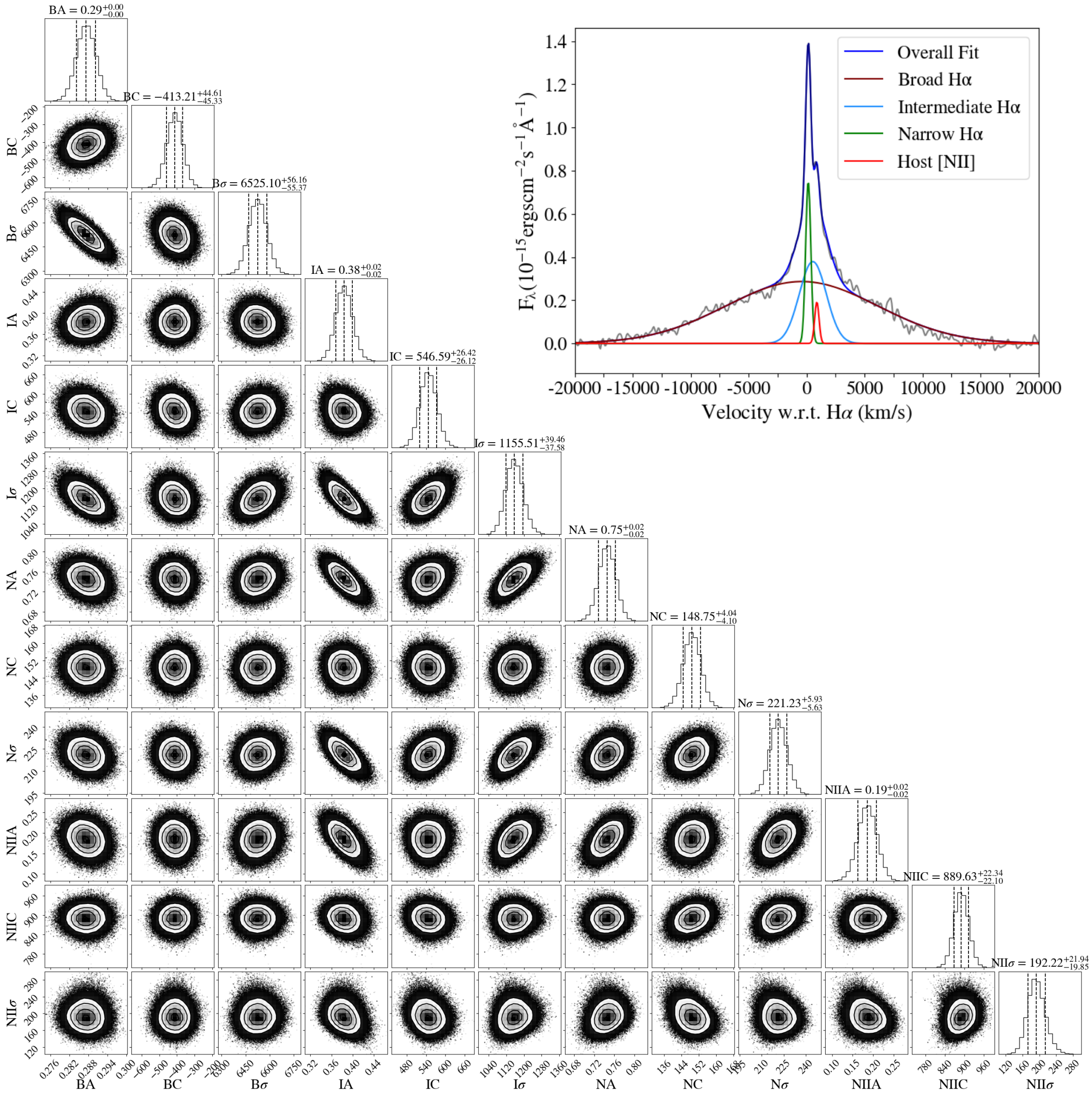

Figure 2. MCMC posteriors and the fitting (with H II region contamination from [N II]) to the first optical spectrum of SN 2020ywx (83 days post-explosion). B, I, N, and NII refer to the broad, narrow, intermediate, and [N II] components of the model. A and C refer to amplitude and central velocity, respectively.

are able to make measurements of the radio mass-loss rate in § 3.

3. INTERPRETATIONS

Having modeled the emission across four wavebands, we now interpret our results to understand the overall picture of SN 2020ywx and its progenitor.

3.1. *X-Ray Interpretation*

Using our X-ray fitting results, we constrain the detailed evolution of SN 2020ywx in the X-rays and place it in context with other X-ray bright SNe IIn. The high temperature across the fits suggests that the X-ray emission must be coming from the forward shock. While the temperature is not fully constrained by our fits, we can use it to approximate the shock velocity as best as possible. Based on our extrapolated values from the temperature evolution we measure, we find that at the first two epochs, the shock speeds were 4100 and 3900 ± 500 $\mathrm{km\,s^{-1}}$ (with error bars found from extrapolating uncertainties in the temperatures at later times). These are somewhat higher than estimates from the FWHM of the intermediate component in the optical Hα fits ($\sim$ 2500–3000 $\mathrm{km\,s^{-1}}$), as expected given that the intermediate component traces the dense shell and not the shock directly. We adopt 4100 $\mathrm{km\,s^{-1}}$ as the shock velocity at 230 days post-explosion when the first X-ray data were taken.

The best-fit power law to the light curve of SN 2020ywx gives a decaying exponential with a decline rate of $0.77^{+0.06}_{-0.06}$. This can be broken down to understand the density structure of the CSM and ejecta. As derived by Fransson et al. (1996) and detailed by Dwarkadas et al. (2016), given an ejecta density profile $\rho_{\rm ej} \approx v^{-n} t^{-3}$ and CSM density profile $\rho_{\rm CSM} \approx r^{-s}$ the luminosity $L \propto t^{-\frac{12-7s+2ns-3n}{n-s}}$

We set our fitted exponent equal to the exponent in the theoretical expression to constrain s and n (Chevalier & Fransson 2017). We fit for a range of $n = 6$–12 as has been seen for many previous SNe (Dwarkadas et al. 2016). We find $s \approx 1.8$–1.9 for our initial range in n. We fix s at 1.85, with $n \approx 6$ (taken with some input from the radio-derived n) suggesting a shallower ejecta/density gradient. It is possible that n < 6 and thus $s \sim 2$ but given the results at radio wavelengths and the discrepancies in CSM densities we eventually measure, we find it more likely that s < 2. We emphasize that this s suggests non-constant mass-loss (Chevalier & Fransson 2017).

To calculate the pre-explosion mass-loss rate from here, we must first determine if the shocks are radiative or adiabatic. This can be done using the derived s and n. We confirm that the X-ray emission is coming from an adiabatic forward shock using equations in (Dwarkadas et al. 2016). We then calculate the mass-loss rate this implies for the progenitor of SN 2020ywx. Fransson et al. (1996) derived that an adiabatic forward shock will have spectral luminosity at 1 keV of

$$L_{\rm CS}(1\ \ {\rm keV}) = \left(\frac{4.1\times10^{37}}{3-s}\right) T_9^{0.16} \times e^{-0.0116/T_9} \xi C_*^2 V_4^{3-2s} \times \left(\frac{t_d}{11.57}\right)^{3-2s}, \tag{2}$$

where t_d is the time since explosion, ξ is related to the chemical composition of the gas (around 0.86 for Solar abundance), and T_9 is the temperature of the shock (which we have constrained along with the shock velocity). We use $s = 1.85$ and the X-ray 0.2–10 keV flux at each epoch to obtain estimates of the luminosity at 1 keV using PIMMS[1]. The result is $C_* = 210$ at the first X-ray epoch, suggesting a mass-loss rate of $(1.3 \pm 0.7) \times 10^{-2}\,{\rm M_\odot\,yr^{-1}}$.

Uncertainties are estimated by propagating errors in the distance, time since explosion, luminosity, and shock speeds (assuming a shock-speed uncertainty of 20% given the uncertainty in the temperature). This mass-loss rate does not change significantly over the following epochs and hovers around $0.01\,{\rm M_\odot\,yr^{-1}}$. This suggests that the star was losing mass at a near-constant rate with no uptick before the explosion, which is surprising for most potential progenitor mechanisms.

3.2. *Optical/IR Interpretation*

Our optical data reveal a linear decline in the *gri*-band light curves. We conclude based on the optical light curve that the mass was lost relatively steadily by the progenitor and there were no varying-density shells of CSM which would potentially produce bumps in the light curve (and would have caused bumps in the radio light curves as well).

We now interpret the spectral fitting results. In the earlier spectra, the lines are best fit by a combination of broad, intermediate, and narrow (in velocity) components as seen in Figure 2. This can be explained through freely expanding ejecta, shocked circumstellar gas, and unshocked photoionized CSM. The intermediate component traces the dense shell between the forward and reverse shocks, and the narrow component comes from the unshocked CSM (Smith 2017).

The broad component of the emission is blueshifted and prominent at early times as was seen in the prototypical SN IIn 2006jd (Stritzinger et al. 2012), which is indicative of asymmetry in the CSM given that we do not necessarily expect to see "through" the photosphere to the freely expanding SN ejecta. This broad component is at $\sim 10,000\,{\rm km\,s^{-1}}$ throughout the early evolution, and it fades at later epochs as one would expect if it originates from freely expanding ejecta.

The intermediate component also decreases in velocity over time, which is unsurprising as the shock and dense shell decelerate. The centroid of the intermediate component additionally shifts bluewards in the spectrum, suggesting dutst blocking emission from the back side of the shell.

3.2.1. *Optical Mass-Loss Rate Calculation*

Now with all the relevant optical parameters calculated, we derive an optical estimate for the mass-loss rate. Given that we lack sufficient UV/IR data (so we cannot truly constrain the bolometric luminosity), we use the Hα luminosity as a proxy for the interaction-driven luminosity contribution for calculating the mass-loss rate. We use the Hα luminosity from the intermediate and broad components (whenever the latter is present — it is mostly weak compared to the intermediate component except at early times) owing to blending between these components in our early-time spectra. As Chugai (1991) showed, the mass-loss rate can then be

---

[1] https://cxc.harvard.edu/toolkit/pimms.jsp

generally written as

$$\dot{M} = \frac{4L_{\mathrm{H}\alpha}v_{\mathrm{w}}}{\epsilon v_{\mathrm{s}}^3}. \tag{3}$$

The shock speed is calculated from the X-ray measurements given that the intermediate line width is both an underestimate of the shock speed and that the line components are likely blended in many of our earlier low-resolution spectra. Here ϵ is related to the efficiency of conversion of kinetic energy to Hα luminosity, and we fix this at 0.1 for these first $\sim 4\,\mathrm{yr}$ post-explosion as is generally expected for a strong The luminosity values are taken from photometric calibrations to our spectra.

At 215 days post-explosion (at the first X-ray epoch), we calculate $\dot{M} = (1.1 \pm 0.4) \times 10^{-2}\,\mathrm{M_\odot\,yr^{-1}}$. There is a general decline in mass-loss rate over the first 1300 days post-explosion to $(2.0 \pm 0.6) \times 10^{-3}\,\mathrm{M_\odot\,yr^{-1}}$. We thus find a non-constant, non-r^{-2} wind density profile for the mass loss; see Figure 3 for the full evolution. Using the relative CSM ($120\,\mathrm{km\,s^{-1}}$) and shock ($\sim 4000\,\mathrm{km\,s^{-1}}$) speeds, we find that the mass loss must have occurred at these elevated rates for at least 100 yr pre-explosion. This duration was determined using $t_{\mathrm{ML}} = (v_{\mathrm{sh}}/v_{\mathrm{CSM}})t$, where t_{ML} refers to the amount of time over which mass was lost.

3.2.2. *Confirmation of Dust from the NIR*

Our NIR spectra are well-fit by blackbodies, which decrease in temperature over time. When combined with the optical blueshift seen, this is definitive evidence for dust in the picture. The blueshift in the optical lines from the shell between the shocks confirms that dust must have formed after the explosion since the location of dust causing the blueshift is internal to the forward shock. This newly formed dust is either in the ejecta or in a dense shell in the post-shock gas. Sarangi & Slavin (2022) argue that in interacting SNe, dust is likely to form in the post-shock gas. Moreover, the blueshift of the optical line profiles is the most prominent if the dust is present close to the line-forming region, in this case the dense shell. The dust is in all likelihood forming in the dense shell where dust formation can happen quite efficiently and at early times (as the blueshift is notable as early as 230 days post-explosion) (Sarangi et al. 2018). Sarangi & Slavin (2022) found that dust formed behind the reverse shock (i.e., not in the ejecta) is much more likely to survive and have a notable effect on the SN line emission out to late times.

3.3. *Radio Interpretation*

Having outlined the radio fitting and analysis process in the previous section, we now interpret our radio results to obtain a third measure of the mass-loss rate. The fact that the radio emission is best described by internal FFA is expected considering the high density of the CSM measured from the X-ray and optical observations.

To find the radio mass-loss rate, we consider the implications of our internal FFA modeling. Weiler et al. (1986) found an expression for the mass-loss rate which we modify for our case considering the early ejecta velocities (found from our earliest optical spectra at 83 days),

$$\begin{aligned}\dot{M} = (2.40 \times 10^{-5})\,\tau_5^{0.5}\left(\frac{v_{\mathrm{w}}}{10\,\mathrm{km\,s^{-1}}}\right)\left(\frac{t_d}{83\,\mathrm{d}}\right)\\ \times\left(\frac{T_e}{10^4\,\mathrm{K}}\right)^{0.68}\mathrm{M_\odot\,yr^{-1}},\end{aligned} \tag{4}$$

where T_e is the electron temperature in the CSM assuming equipartition between ions and electrons, and τ_5 is the 5 GHz optical depth as found from the internal FFA model. Given the unequivocally high measured mass loss, we assume that the CSM is not preionized and thus that the initial CSM temperature is the standard $10^5\,\mathrm{K}$. At later epochs, we assume that the wind temperature decreases to around $10^4\,\mathrm{K}$. At the initial radio epoch at 400 days, we derive a mass-loss rate of $(8.9 \pm 2.5) \times 10^{-3}\,\mathrm{M_\odot\,yr^{-1}}$. Under the assumption that the electron temperature decreases linearly over time, the mass-loss rate was gradually increasing in the decades before the explosion and was at $(4.3 \pm 2.0) \times 10^{-3}\,\mathrm{M_\odot\,yr^{-1}}$ in the final epoch of radio observations which trace 100 yr before the explosion. This suggests a nonconstant $s \neq 2$ evolution of the density profile, similar to the optical and X-ray results, although the decline differs from the X-ray results. The full radio mass-loss results are shown in Figure 3.

4. DISCUSSION

The three wavelengths of data across epochs paint a consistent picture for SN 2020ywx: sustained mass loss around 10^{-3}–$10^{-2}\,\mathrm{M_\odot\,yr^{-1}}$ over at least 100 yrs pre-explosion. However, there are differences across wavelengths, particularly between the X-rays and other wavelengths, which point to asymmetries. In more detail, the results support an asymmetric CSM with extensive CSM/clumps along certain regions around the star and lesser CSM density in other areas. We may be receiving X-ray emission from certain denser inner regions with radio emission from outer faster-moving regions. We note that given the shock and wind speed and average mass-loss rate measured, we are in a regime when our data were taken when the wind optical depth $\tau_w \approx 1$ (Chevalier & Irwin 2012), and thus in a regime where the X-ray emission should be maximized and not suffer heavily from photoabsorption and other cooling effects. As we lack higher-resolution radio data data, we cannot confirm this picture for the radio emission coming from faster-moving less dense material, but this is a scenario that was seen in SN 2014C with similar elevated X-ray luminosity (Brethauer et al. 2022).

It would not be surprising, based on the evolution so far, if this SN were to remain bright for years to come and thus suggest a very high-mass progenitor. The mass-loss rate derived for SN 2020ywx, as was the case for SN 2010jl and many other SNe IIn, defies the conventional values found for wind-driven steady mass loss which reaches its limits around $10^{-4}\,\mathrm{M}_\odot\,\mathrm{yr}^{-1}$ (Smith 2014).

We consider the possibility of eruptive mass loss from an LBV-like star or cool supergiant. For an LBV-like star, the eruptive event is expected to last a few years to a decade as seen observationally (e.g., Smith et al. 2011b), while for a cool hypergiant, it can last for hundreds of years (Smith 2014). The evolution of the optical light curve in particular does not lend credence to the idea of repeated outbursts from a single star given that if there were shells with varying densities, there would be less of a constant decline in the light curve. We note, however, that LBVs can eject bipolar/aspherical shells with a wide range of speeds and CSM at a large range of radii, even from a single event. A hypergiant could sustain high mass loss for more extended periods (Smith 2014). However, the derived CSM speed ($\sim 100\,\mathrm{km\,s^{-1}}$) exceeds the boundaries of the expected wind speed for these red supergiants or yellow hypergiants (Goldman et al. 2017). Thus, yellow hypergiant mass loss seems unlikely as the explanation for the progenitor of SN 2020ywx. Other proposed channels include wave-driven mass loss and burning instabilities (Quataert & Shiode 2012; Smith & Arnett 2014) as well as enhanced red supergiant mass loss (Yoon & Cantiello 2010). However, the timescales for wave driving are too short (on the scale of around a year) to explain the long-lasting ($> 100\,\mathrm{yr}$) mass loss in SN 2020ywx. For other nuclear-burning instabilities, the presence of strong Hydrogen in nearby CSM disfavors this hypothesis. For enhanced red supergiant winds, the measured wind speed is still much too high.

We thus consider the possibility of binary-driven mass loss as perhaps the only mechanism that can explain the quantity and duration of mass loss derived across all wavelengths (Smith & Arnett 2014). First, the non-uniformity ($s \neq 2$) suggested by our mass-loss measurements and the presence of broad ejecta from early times in the spectra suggests a binary progenitor mechanism, as single stars would not generally be expected to lose mass in such a non-geometrically-uniform way (although there may be exceptions for rapid rotators). In other words, there must be some pockets of low optical depth that allow us to see "through" the highly dense CSM which are difficult to explain under single-star mass loss. It has become clear that binarity has a far more important role to play than previously thought for massive stars (Sana et al. 2012), and binarity leading to a merger (which is also plausible here) has been suggested as a possible progenitor mechanism for other SNe IIn such as SN 2015da (Smith et al. 2023), SN 2014C (Thomas et al. 2022), or SN 2001em given common-envelope evolution (Chandra et al. 2020). In this context, it is worth remembering that LBV eruptions, often invoked to account for the CSM of SNe IIn, may themselves be a binary interaction phenomenon. The best example is the massive LBV star η Carinae, for which a binary merger is the leading explanation for its eruption (Smith et al. 2018). Binary evolution in the form of Roche-lobe overflow could explain the very dense H-rich CSM formed while also accounting for the $100\,\mathrm{km\,s^{-1}}$ speed at which the material was lost and the timescale.

5. CONCLUSIONS

Through an exploration of the radio, NIR, optical, and X-ray emission of the Type IIn SN 2020ywx, we obtained three independent estimates of the mass-loss rate for the progenitor of SN 2020ywx. This was made possible by combining high-resolution spectral measurements in the optical with data in the radio and X-rays. All three values were found to be relatively consistent and suggestive of extreme mass loss (at $\sim 10^{-2}\,\mathrm{M}_\odot\,\mathrm{yr}^{-1}$) for at least a century preceding the explosion. However, the differences in mass-loss calculated across wavelengths suggest asymmetries in the CSM. In more detail, this work has provided a variety of insights regarding SN 2020ywx, as follows:

1. From the X-ray luminosity evolution of SN 2020ywx, we calculate values for the mass-loss rate across time. There is a plateau in the X-ray mass-loss rate, which does not match results at other wavelengths. We thus suggest that the X-ray emission originates in a dense region of CSM.

2. The high-resolution optical spectra show P Cygni profiles in the narrow lines, which directly constrain the CSM speed at $120 \pm 22\,\mathrm{km\,s^{-1}}$.

3. Using the Hα luminosity, we derive a declining optical mass-loss rate around $10^{-2}\mathrm{M}_\odot\mathrm{yr}^{-1}$ over 100 years pre-explosion for the progenitor of SN 2020ywx.

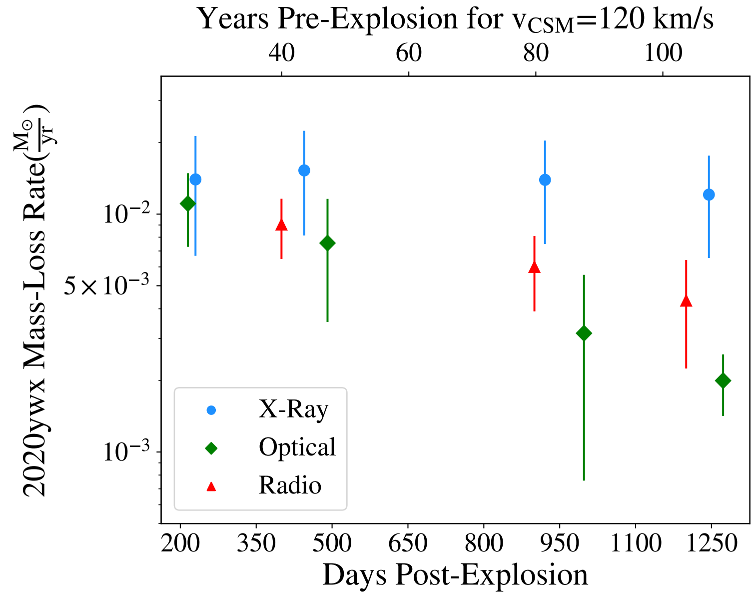

Figure 3. Mass-loss rate constrained across wavelengths at epochs for which we have data in each band. The mass loss is consistently high at $\sim 0.01\,M_\odot\,yr^{-1}$ and persists near this rate for close to 100 yr (with this time frame measured through the relative speed of the shock to the CSM) at each wavelength. We note the discrepancy at late times between the X-rays and the radio/optical results, which we ascribe to asymmetries in the CSM.

4. The NIR spectra show additional emission lines of hydrogen and helium. The continuum is well fit by a 1000 K blackbody which is indicative of formation of new dust and its evolution.

5. The derived radio optical depth from modeling shows a mass-loss rate declining over time, assuming the expected decrease in electron temperature. This again suggests $s \neq 2$ and confirms asymmetric mass loss.

We explore different progenitor channels and conclude that binary interaction is the most plausible channel that can explain the overall mass-loss picture of SN 2020ywx. This is another case that adds to the consensus that SN IIn progenitors are diverse and complex. We emphasize the importance of obtaining both low-frequency radio data, and high-resolution optical/X-ray spectra for IIn SNe to fully constrain the mass-loss history.

6. ACKNOWLEDGMENTS

R.B.-W. and P.C. acknowledge NASA award GO3-24056X. R.B.-W. acknowledges support from a VSGC Fellowship. M.M. and the METAL group at UVa acknowledge support in part from ADAP program grant 80NSSC22K0486, from NSF grant AST-2206657, and from *HST* program GO-16656.

Facilities: GMRT, VLA, LBT, MMT, Lick Observatory, Keck, LCO, Chandra, Swift (XRT)

REFERENCES

Aghakhanloo, M., Smith, N., Milne, P., et al. 2023, MNRAS, 526, 456, doi: 10.1093/mnras/stad2702

Bilinski, C., Smith, N., Williams, G. G., et al. 2024, MNRAS, 529, 1104, doi: 10.1093/mnras/stae380

Brethauer, D., Margutti, R., Milisavljevic, D., et al. 2022, ApJ, 939, 105, doi: 10.3847/1538-4357/ac8b14

Chandra, P. 2018, SSRv, 214, 27, doi: 10.1007/s11214-017-0461-6

Chandra, P., Chevalier, R. A., Chugai, N., Milisavljevic, D., & Fransson, C. 2020, ApJ, 902, 55, doi: 10.3847/1538-4357/abb460

Chevalier, R. A. 1982, ApJ, 259, 302, doi: 10.1086/160167

Chevalier, R. A., & Fransson, C. 2017, in Handbook of Supernovae, ed. A. W. Alsabti & P. Murdin (Springer), 875, doi: 10.1007/978-3-319-21846-5_34

Chevalier, R. A., & Irwin, C. M. 2012, ApJL, 747, L17, doi: 10.1088/2041-8205/747/1/L17

Chugai, N. N. 1991, MNRAS, 250, 513, doi: 10.1093/mnras/250.3.513

Chugai, N. N., & Danziger, I. J. 1994, MNRAS, 268, 173, doi: 10.1093/mnras/268.1.173

Cold, C., & Hjorth, J. 2023, A&A, 670, A48, doi: 10.1051/0004-6361/202244867

Dessart, L., & Hillier, D. J. 2022, A&A, 660, L9, doi: 10.1051/0004-6361/202243372

Dwarkadas, V. V., Romero-Cañizales, C., Reddy, R., & Bauer, F. E. 2016, MNRAS, 462, 1101, doi: 10.1093/mnras/stw1717

Filippenko, A. V. 1997, ARA&A, 35, 309, doi: 10.1146/annurev.astro.35.1.309

Foreman-Mackey, D., Hogg, D. W., Lang, D., & Goodman, J. 2013, PASP, 125, 306, doi: 10.1086/670067

Fox, O. D., Chevalier, R. A., Skrutskie, M. F., et al. 2011, ApJ, 741, 7, doi: 10.1088/0004-637X/741/1/7

Fransson, C., Lundqvist, P., & Chevalier, R. A. 1996, ApJ, 461, 993, doi: 10.1086/177119

Gal-Yam, A., Yaron, O., Pastorello, A., et al. 2021, Transient Name Server AstroNote, 76, 1

Gal-Yam, A., Leonard, D. C., Fox, D. B., et al. 2007, ApJ, 656, 372, doi: 10.1086/510523

Gall, C., Hjorth, J., Watson, D., et al. 2014, Nature, 511, 326, doi: 10.1038/nature13558

Goldman, S. R., van Loon, J. T., Zijlstra, A. A., et al. 2017, MNRAS, 465, 403, doi: 10.1093/mnras/stw2708

Heger, A., Fryer, C. L., Woosley, S. E., Langer, N., & Hartmann, D. H. 2003, ApJ, 591, 288, doi: 10.1086/375341

Margalit, B., Quataert, E., & Ho, A. Y. Q. 2022, ApJ, 928, 122, doi: 10.3847/1538-4357/ac53b0

Mauerhan, J. C., Smith, N., Filippenko, A. V., et al. 2013, MNRAS, 430, 1801, doi: 10.1093/mnras/stt009

Modjaz, M., Gutiérrez, C. P., & Arcavi, I. 2019, Nature Astronomy, 3, 717, doi: 10.1038/s41550-019-0856-2

Quataert, E., & Shiode, J. 2012, MNRAS, 423, L92, doi: 10.1111/j.1745-3933.2012.01264.x

Reguitti, A., Pignata, G., Pastorello, A., et al. 2024, arXiv e-prints, arXiv:2403.10398, doi: 10.48550/arXiv.2403.10398

Sana, H., de Mink, S. E., de Koter, A., et al. 2012, Science, 337, 444, doi: 10.1126/science.1223344

Sarangi, A., Dwek, E., & Arendt, R. G. 2018, ApJ, 859, 66, doi: 10.3847/1538-4357/aabfc3

Sarangi, A., & Slavin, J. D. 2022, ApJ, 933, 89, doi: 10.3847/1538-4357/ac713d

Schlegel, E. M. 1990, MNRAS, 244, 269

Smith, N. 2014, ARA&A, 52, 487, doi: 10.1146/annurev-astro-081913-040025

Smith, N. 2017, Interacting Supernovae: Types IIn and Ibn (Springer International Publishing), 403–429, doi: 10.1007/978-3-319-21846-5_38

Smith, N., Andrews, J. E., Milne, P., et al. 2023, arXiv e-prints, arXiv:2312.00253, doi: 10.48550/arXiv.2312.00253

Smith, N., & Arnett, W. D. 2014, ApJ, 785, 82, doi: 10.1088/0004-637X/785/2/82

Smith, N., Li, W., Filippenko, A. V., & Chornock, R. 2011a, MNRAS, 412, 1522, doi: 10.1111/j.1365-2966.2011.17229.x

Smith, N., Li, W., Silverman, J. M., Ganeshalingam, M., & Filippenko, A. V. 2011b, MNRAS, 415, 773, doi: 10.1111/j.1365-2966.2011.18763.x

Smith, N., & Owocki, S. P. 2006, ApJL, 645, L45, doi: 10.1086/506523

Smith, N., & Tombleson, R. 2015, MNRAS, 447, 598, doi: 10.1093/mnras/stu2430

Smith, N., Li, W., Foley, R. J., et al. 2007, ApJ, 666, 1116, doi: 10.1086/519949

Smith, N., Andrews, J. E., Rest, A., et al. 2018, MNRAS, 480, 1466, doi: 10.1093/mnras/sty1500

Srivastav, S., Smith, K. W., McBrien, O., et al. 2020, Transient Name Server AstroNote, 215, 1

Stritzinger, M., Taddia, F., Fransson, C., et al. 2012, ApJ, 756, 173, doi: 10.1088/0004-637X/756/2/173

Taddia, F., Stritzinger, M. D., Sollerman, J., et al. 2013, A&A, 555, A10, doi: 10.1051/0004-6361/201321180

Thomas, B. P., Wheeler, J. C., Dwarkadas, V. V., et al. 2022, ApJ, 930, 57, doi: 10.3847/1538-4357/ac5fa6

Weiler, K. W., Sramek, R. A., Panagia, N., van der Hulst, J. M., & Salvati, M. 1986, ApJ, 301, 790, doi: 10.1086/163944

Woosley, S. E. 2017, ApJ, 836, 244, doi: 10.3847/1538-4357/836/2/244

Woosley, S. E., & Smith, N. 2022, ApJ, 938, 57, doi: 10.3847/1538-4357/ac8eb3

Wu, S., & Fuller, J. 2021, ApJ, 906, 3, doi: 10.3847/1538-4357/abc87c

Yesmin, N., Pellegrino, C., Modjaz, M., et al. 2024, arXiv e-prints, arXiv:2409.04522, doi: 10.48550/arXiv.2409.04522

Yoon, S.-C., & Cantiello, M. 2010, ApJL, 717, L62, doi: 10.1088/2041-8205/717/1/L62